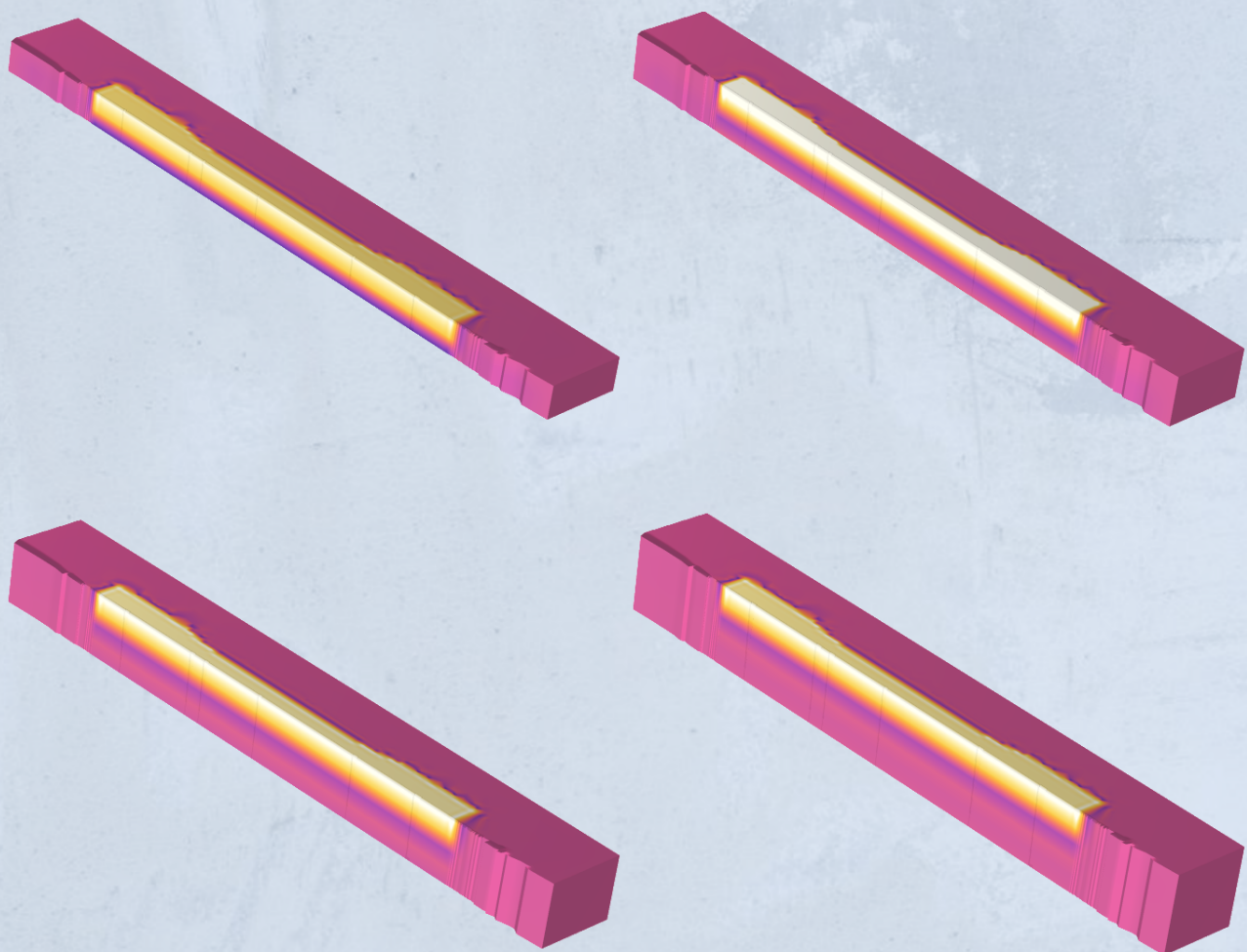


Development of a Thermal Model for SLS Printing Using a Flash Heating Approach

Preproject for the Master's Degree of
Anton Østergaard Thorsen



This page is intentionally left blank.

Development of a Thermal Model for SLS Printing Using a Flash Heating Approach

by

Anton Østergaard Thorsen

Name	Position	Student Number	Contacts
Anton Østergaard Thorsen	Master Student in Mechanical Engineering	202004932	anton-thorsen@hotmail.com
Supervisor	Position	-	Contacts
Michael Sandberg	Tenure Track Assistant Professor Aarhus University	-	ms@mpe.au.dk
Co-Supervisors	Posisiton	-	Contacts
Michal Budzik	Associate Professor Aarhus University	-	mibu@mpe.au.dk

University: Aarhus University
Department: Department of Mechanical and Production Engineering
Project Duration: August, 2024 – December, 2024

Last Compiled: December 6, 2024



DEPARTMENT OF MECHANICAL AND PRODUCTION ENGINEERING
AARHUS UNIVERSITY

Abstract

This study aimed to develop a flash heating model for the Selective Laser Sintering (SLS) process. The resulting model is user-friendly and can be easily adapted to address specific thermal problems for various geometries and material properties. The model incorporates critical phase changes occurring during SLS printing, including the effects of thermal hysteresis, as well as the effects of viscosity, porosity, and crystallinity that influence material properties.

To ensure the model's robustness and computational efficiency, a thorough evaluation of various parameters was conducted. These parameters included the type of heat source, mesh discretization, heat exposure time, mesh refinement in the build plane and build direction and the number of layers in the printing process. These investigations were conducted with the long-term goal of extending the model's capabilities to predict residual stresses. The study found that the model is highly robust, producing peak layer temperature within a few degrees across most parameter variations. To get a sense of the computational time it would require to achieve sufficiently refined residual stress results in future work, an optimized configuration was identified. This configuration includes a smoothed square wave heat source, linear discretization, an extended heat exposure time (from $t_{heat} = 0.0012\text{ s}$ to $t_{heat} = 0.012\text{ s}$), a fine mesh, and a layer height of 0.4 mm. This setup achieves a simulation time of 26 minutes and 53 seconds on a laptop.

Table of Contents

Abstract	i
Table of Contents	ii
List of Figures	iii
List of Tables	iv
Nomenclature	vi
1 Introduction to SLS	1
2 Background Theory	5
2.1 Governing Equations	5
2.1.1 Material properties in SLS	9
2.1.2 Thermal Hysteresis	10
2.2 Flash Heating Simulation	13
2.2.1 Applied Heat Source	13
2.2.2 Controlling the Position of the Laser	14
2.2.3 Meshing and Time-stepping	17
3 Results and Discussion	20
3.1 Simulation Setting Analysis	24
4 Future work	30
5 Conclusion	31
6 Bibliography	33

List of Figures

1.1 Schematic of SLS print-process	2
2.1 Schematic of SLS process and the boundary conditions of the heating phase	7
2.2 Boundary conditions in the cooling phase of the SLS print-process	8
2.3 Hysteresis of PA-12	11
2.4 Hysteresis path of layer of PA12 in SLS print	12
2.5 The three different heat sources in time investigated in the simulations	14
2.6 ASTM D638 tensile test specimen	15
2.7 Cross-sectional area in the build-direction	15
2.8 Position of laser over time in build direction	16
2.9 ASTM D638 oriented as simulated	17
2.10 Coarse mesh without dogbone	18
2.11 Mesh for identity mapping	18
2.12 Top view of 3D mesh: Fine mesh without dogbone	18
3.1 Section-view of the layer-by-layer temperature distribution of the flash heating process for 4 layers in total. The x -axis has been scaled by a factor of 7 for visual clarity	20
3.2 Heating phase temperature at the center of every layer of the baseline simulation. Each layer is plotted from the time just before the layer is activated to the end time. That is why only the first layer is active at $t = 0$	21
3.3 Heating & cooling phase temperature at center of every layer of the baseline simulation	22
3.4 Temperature over time of third layer	23
3.5 Hysteresis path of layer 3. The hysteresis is being reset from point 3 to point 4	23
3.6 Results for the first four settings in the settings analysis	25
3.7 Results for the last four settings in the settings analysis	26
3.8 Section view of the density in the 'Optimized geometry'. The x -direction is scaled with a factor of 5	27

List of Tables

3.1 Results for every simulation. *The optimized geometry consists of Q_{smooth} , linear discretization, $t_{heat} = 0.012$ s, fine meshing, 1 element in build direction, and $N_o = 8$	27
---	----

Nomenclature

Physics Constants

σ	Stefan-Boltzmann constant	$5.67 \times 10^{-8} \text{ W m}^{-2} \text{ K}^{-4}$
R	Universal gas constant	$8.314 \text{ J mol}^{-1} \text{ K}^{-1}$

Symbols related to viscosity, crystallinity & porosity

β	Crystalline coefficient	—
χ	Crystalline fraction	—
η	Viscosity growth rate	s^{-1}
η_0	Pre-exponential factor	s^{-1}
ϕ	Porosity	—
ζ	Retardation due to crystallization	—
E_a	Activation energy	kJ mol^{-1}

Thermal Symbols

α	Thermal diffusivity	$\text{m}^3 \text{ s}^{-1}$
ρ	Density	kg m^{-3}
ε	Emissivity	—
ξ	Absorptivity	—
c_p	Specific heat capacity	$\text{J kg}^{-1} \text{ K}^{-1}$
h	Enthalpy	J kg^{-1}
h_c	Heat transfer coefficient	$\text{W m}^{-2} \text{ K}^{-1}$

NOMENCLATURE

k	Thermal conductivity	$\text{W m}^{-1} \text{K}^{-1}$
Q	Heat flow rate	W
q	Heat flux	W m^{-3}
T	Temperature	$^{\circ}\text{C}$

Other Symbols

δ	Layer height	μm
H	Hatch spacing	mm
t	Time	s
V	Velocity	m s^{-1}
CSA	Cross-sectional area	m^2

1 | Introduction to SLS

Many traditional manufacturing methods often face significant challenges when used to produce complex parts. Intricate geometries, internal channels, and custom features can require expensive tooling, multi-step processes, or even design compromises to make them manufacturable. These limitations not only increase production costs but also restrict design freedom. Additive Manufacturing (AM), offers a transformative solution to these challenges. By building parts layer by layer directly from a digital model, AM eliminates the need for molds, specialized tools, or assembly of subcomponents. Engineers can design highly complex structures, that would be impossible or prohibitively expensive with traditional techniques. With AM, complexity no longer adds significant manufacturing cost, enabling designers to focus on optimizing performance, weight, or functionality without worrying about production constraints. This makes AM beneficial for industries such as the aerospace-, medical-, and automotive industries, where custom, high-performance, or lightweight components are essential [16].

Selective Laser Sintering

This study focuses on selective laser sintering (SLS) which is an AM method, that is based on the sintering of nonmetallic powders. Sintering is the process of fusing powder without fully melting the material. SLS offers some notable advantages compared to other AM methods, including generally isotropic material properties and strong mechanical performance, and for polymers, no additional support structures are typically required. As SLS can achieve dimensional tolerances of ± 0.1 mm, it is quite suitable for applications requiring precision. However, the process has its drawbacks, including high machine costs (ranging from \$300,000 to \$1 million), and like many other AM processes, it faces challenges when used for large-scale production. As such it is best in custom, low-scale production or for prototyping [11, Section 20.6.1].

Materials for SLS

Thermoplastics are ideal for SLS due to their low melting temperatures, which reduce laser power requirements. In contrast, thermoset polymers are unsuitable, as they degrade rather than melt. The crystallinity of thermoplastics plays a critical role in process reliability. Amorphous polymers, characterized by randomly arranged molecular chains, melt

over a wide temperature range that tends to result in the part failing to form well-defined features. Semi-crystalline thermoplastics, such as Polyamide 12 (PA12), melt at a well-defined temperature and yield stronger, higher-density parts. However, semi-crystalline polymers are prone to shrinkage and distortion, making uniform temperature control crucial to prevent uneven shrinkage [8, Section 5.2.1].

Build Chamber and Mechanisms

This study will be based on printing with PA12 on the Lisa X SLS printer by Sinterit. The SLS process takes place within a controlled environment called the process chamber where, initially, the temperature of the powder is just below the material's melting temperature.

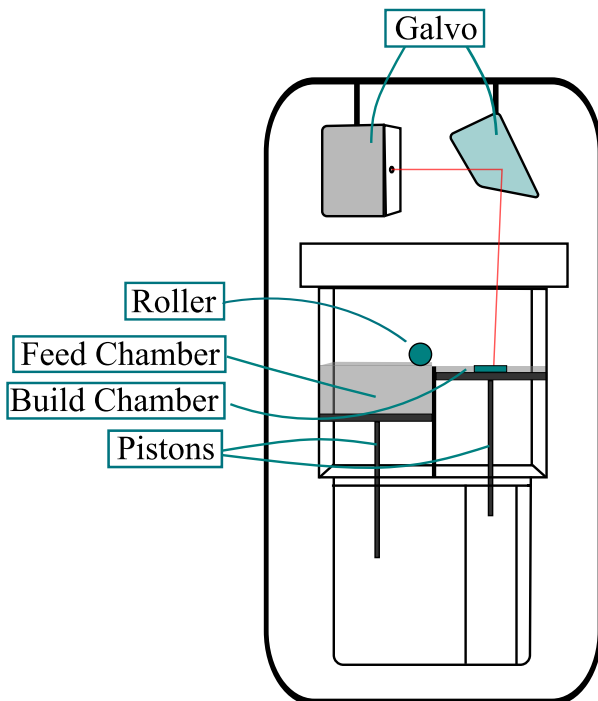


Figure 1.1 | Schematic of SLS print-process

Inside, a build platform holds the powder bed, while a powder-feed platform connected to a motorized system deposits new powder layers (typical layer thickness is 75-175 μm). A

roller mechanism distributes the powder evenly across the build platform. A laser, guided by a galvanometer (a system of controllable mirrors), selectively sinters the powder into the desired geometry, and to ensure optimal processing conditions, an infrared heater warms the top powder layer. Normally an environmental control unit supplies nitrogen to prevent oxidation, but when printing with PA12 on the Lisa-X the supply of nitrogen is not required [19, 20]. After printing, the part must cool gradually to avoid warping, which can occur due to uneven thermal contraction. In extreme cases, this warping may result in collisions with the powder roller, compromising the build quality [11, Section 20.6.1] [8, Section 5-1].

Simulation Methods for SLS

Several approaches exist for simulating layer-by-layer additive manufacturing processes like SLS. The choice of simulation method depends on the desired level of accuracy and computational efficiency [1].

1. Laser Scan Pattern Simulation (Micro-Scale):

This method involves simulating the laser's actual scan path, requiring precise movements in the x , y , and z directions. While this approach provides the highest fidelity and captures fine details of the process, it is computationally expensive. As a result, it is primarily used for micro-scale simulations, such as simulating a single pass of the laser.

2. Flash Heating (Macro-Scale):

Flash heating is a more computationally efficient alternative, particularly suited for simulating entire parts. In this method, an entire layer is activated and heated simultaneously. All layers below the active layer are "alive" (i.e., thermally active), while those above remain deactivated. Once the active layer is heated, the simulation progresses to the next layer in the build direction. Heating every particle in a layer simultaneously is a simplification of the real process, however, it significantly reduces computational costs, making it viable for certain macro-scale simulations.

3. Sequential Flash Heating (Meso-Scale):

This method strikes a balance between fidelity and computational efficiency. Sequential flash heating divides each layer into stripes. The laser heats one stripe at a time within the active layer, moving sequentially to the next stripe. After all the stripes in a layer are heated, the simulation advances to the next layer in the build direction. By simulating stripe-wise activation, this approach captures more in-layer detail than flash heating while remaining less computationally demanding than full laser scan simulations [1].

Each of these methods has its strengths and weaknesses, making them suitable for different scales and levels of process detail.

CHAPTER 1. INTRODUCTION TO SLS

This study investigates the applicability of using a flash heating model to simulate the thermal behavior and density changes in an SLS-print. It builds on prior research into the simulation of SLS processes. Zhang et al. [22] utilized an in-house software, LBPF-Sim, which leveraged parallel computing and adaptive meshing to simulate multi-line and full SLS parts with scanning patterns. Riedlbauer et al. [15] investigated the melt pool formation during single-line SLS printing through both experimental and numerical approaches. Shen et al. [17] developed a thermomechanical model for a single layer of an SLS-printed part, calculating its elastic, viscoplastic, thermal, and residual stresses, and validated their model experimentally. Bayat et al. [1] proposed a thermomechanical model using flash heating and sequential flash heating for SLM components.

The flash heating model will take into account the effect that changes in viscosity, crystallinity, and porosity have on the density. The goal is to develop an efficient, easy-to-use flash heating model. This model aims to reduce computational time, enabling the simulation of multiple parts and even entire build chambers. This approach will lay the foundation for the author's Master's thesis, which focuses on residual stresses in SLS. By developing an efficient thermal model, it will become easier to understand the thermal effects that contribute to residual stress formation. Ultimately, the goal is to experimentally validate the results, providing a more comprehensive understanding of residual stresses in 3D-printed components and advancing the field of additive manufacturing.

2 | Background Theory

2.1 | Governing Equations

To model the distribution and flow of temperature within a medium as it varies over space and time the heat equation is used [Section 2-3, [3]]

$$\frac{\partial}{\partial x} \left(k \frac{\partial T}{\partial x} \right) + \frac{\partial}{\partial y} \left(k \frac{\partial T}{\partial y} \right) + \frac{\partial}{\partial z} \left(k \frac{\partial T}{\partial z} \right) + q_V = \rho c_p \frac{\partial T}{\partial t} \quad (2.1)$$

Heat conduction in one dimension is given in Eq. 2.2 [Section 1-5, [3]]

$$q_{cond} = -k \frac{dT}{dx} \quad (2.2)$$

As such the first three terms on the left-hand side of Eq. 2.1 include the heat conduction in the x -, y -, and z -direction respectively, where k is the thermal conductivity of the material which has the unit [$\text{W m}^{-1} \text{K}^{-1}$]. The last term on the left-hand side q_V is the volumetric heat source that has the unit [W/m^3], which accounts for the heat sources within the medium.

The term on the right-hand side is the time-dependent term and as such it represents the change of thermal energy with time. Here ρ is the density which has the unit [kg/m^3] and c_p is the specific heat capacity that describes the amount of energy needed to raise the temperature of one kilogram by one kelvin, it has the unit [$\text{J kg}^{-1} \text{K}^{-1}$]

The partial derivative terms on the left hand side represent the temperature gradient in each spatial direction, and by squaring the sum of these terms the Laplacian is obtained:

$$\nabla^2 T = \frac{\partial^2 T}{\partial x^2} + \frac{\partial^2 T}{\partial y^2} + \frac{\partial^2 T}{\partial z^2} \quad (2.3)$$

Using the Laplacian the heat equation can be written in short-form

$$\rho c_p \frac{\partial T}{\partial t} + \nabla(-k \nabla T) = q_V \quad (2.4)$$

In SLS-print, initially, the material is a powder. As such how heat transfers through the powder depends on the porosity as the heat in reality has to travel through both the

material and air. A simple model to describe the thermal conductivity as a function of the porosity is [9],

$$k_{powder}(\phi) = k_{solid}(1 - \phi) \quad (2.5)$$

The thermal conductivity of solid PA12 is $0.23 \text{ W m}^{-1} \text{ K}^{-1}$ [14]. This expression neglects any heat transfer of the air packed between the particles. Note that Eq. 2.5 is the upper bound of the Rule of Mixtures, and the true thermal conductivity lies somewhere between the upper bound and the lower bound. [Section 3, [10]].

The porosity in Eq. 2.5 depends on the density [6]

$$\phi(\rho) = \frac{\rho_{solid} - \rho}{\rho_{solid}} \quad (2.6)$$

The density for solid PA12, ρ_{solid} , is 1030 kg m^{-3} and for loose PA12 powder, the porosity is $\phi_i = 0.51$ [18].

Both convection and radiation boundary conditions will be present. Convection is given by Eq. 2.7 [Section 1-7, [3]]:

$$q_{conv} = \hat{n}(k\nabla T) = h_{tc}(T_s - T_\infty) \quad (2.7)$$

And the equation for radiation is [Section 1-8, [3]]:

$$q_{rad} = \hat{n}(k\nabla T) = \varepsilon\sigma(T_s^4 - T_\infty^4) \quad (2.8)$$

Eqs. 2.1 to 2.8 govern the thermal problem addressed in this study. Note that two phases of the thermal problem will be considered, first a heating phase where the part is created, and then a cooling phase where the machine is turned off and the part allowed to cool to room temperature. The boundary conditions change depending on the phase. The boundary conditions of the heating phase are illustrated in Fig. 2.1.

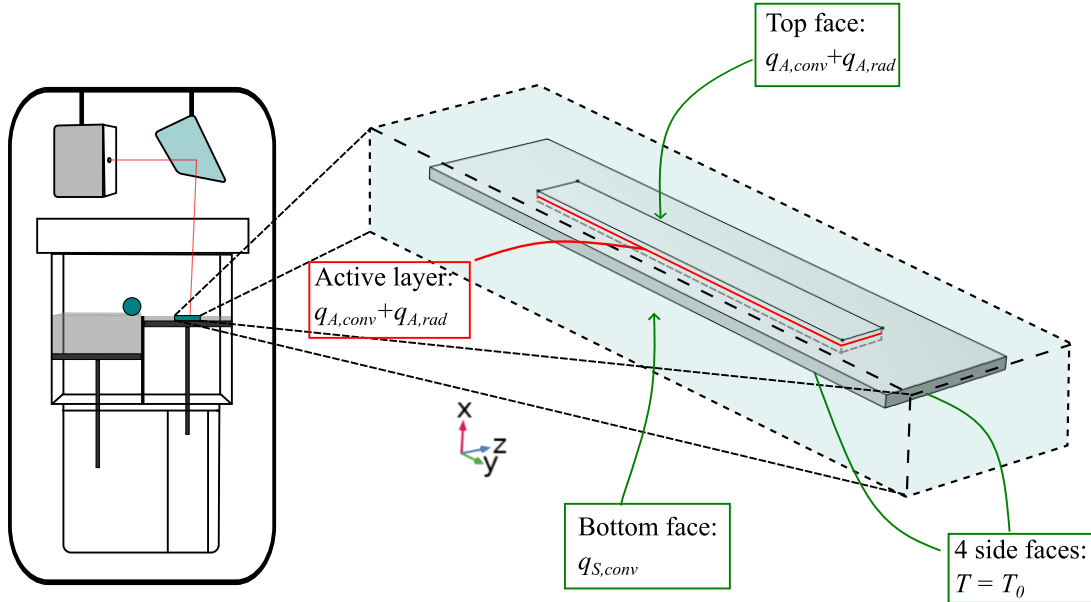


Figure 2.1 | Schematic of SLS process and the boundary conditions of the heating phase

Within the dashed, opaque region in Fig. 2.1 a thin rectangular box with an embedded smaller box is illustrated. The embedded smaller box represents the build region, marked by a red line, which is the region that is affected by the laser, and where the chosen part, an ASTM D638 tensile test specimen, is created. The area outside the build region is the powder region, which contains the powder that is unaffected by the laser. This allows heat from the build region to diffuse into the powder region. The heating phase has the following boundary conditions:

- On the bottom face, an artificial convection boundary condition is applied. It is artificial in the sense that in reality, this face doesn't convect heat, but instead, it conducts heat through the metal bottom of the build chamber. Chao Li, et al. have determined an artificial heat transfer coefficient for simulation-use for the sides of a similar SLS-printer to be $10 \text{ W m}^{-2} \text{ K}^{-1}$ [13]
- On the side faces Dirichlet boundary conditions are applied to enforce the temperature to be equal to the initial temperature of the powder $T_0 = 175^\circ\text{C}$. This assumes that the powder region is large enough so that the sides are far enough away from the build region so they are not affected by the heating.
- On the top face both convection and radiation boundary condition applies. Based

on [12] the heat transfer coefficient with the free air is set to be $15 \text{ W m}^{-2} \text{ K}^{-1}$, and the emissivity is 0.8 based on [14].

- On the active layer the heat source is applied as well as a convection and radiation boundary condition equal to that of the top face.

To ensure that the bottom boundary condition is not applied directly to the part, a single layer of powder is modeled between the bottom face and the build region. Similarly on the top face, to ensure that the convection and radiation boundary condition of both the active layer and the top face is not applied simultaneously on the final layer, a single buffer layer of air in between the top face and the build region is added.

During the heating phase the ambient temperature T_∞ is 175°C , however, once the cooling phase begins, the ambient temperature will be changed to 20°C for the simulation. Note that this is a gross simplification as the temperature doesn't suddenly change from 175°C to 20°C , instead it ramps down. How exactly it ramps down in the Lisa-X printer will be a task for future work, as such the cooling phase in this study is more of a proof-of-concept.

Fig. 2.2, shows the boundary conditions in the cooling phase. For the cooling phase, the powder region is enlarged to capture all the powder in the build chamber. This is necessary as the amount of powder affects how quickly the part cools down. This is vital for future work when the residual stresses need to be modeled.

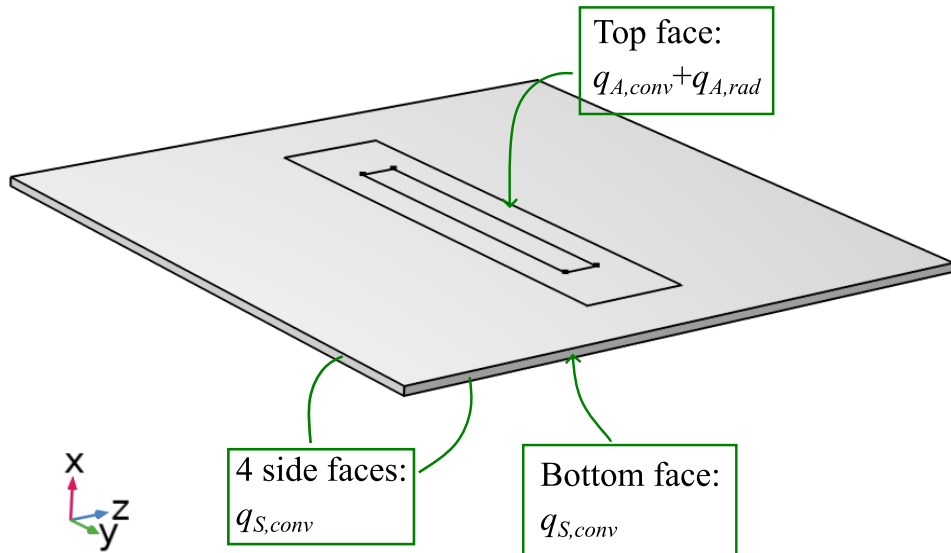


Figure 2.2 | Boundary conditions in the cooling phase of the SLS print-process

Since the side faces are now in direct contact with the build chamber, the boundary conditions of the side faces become equal to that of the bottom face. The boundary condition of the top face remains unchanged compared to the heating phase.

2.1.1 | Material properties in SLS

As the powder sinters the density changes. How the density of a crystalline polymer is affected relies on multiple things, among which is the viscosity, which for SLS can be described by the relation in Eq. 2.9 [4],

$$\eta = \eta_0 \exp\left(-\frac{E_A}{RT}\right) \quad (2.9)$$

Where $\eta_0 = 5 \times 10^{13} \text{ s}^{-1}$, is a pre-exponential factor [9], $E_A = 102 \text{ kJ mol}^{-1}$ is the activation energy, which is the energy required for the flow to occur, or more specifically, the energy required to overcome the molecular interactions that determine the viscosity [21]. $R = 8.314 \text{ J mol}^{-1} \text{ K}^{-1}$ is the ideal gas constant.

PA12 is a semi-crystalline polymer and for that reason, retardation, which is a delay or hindrance, as the polymer crystallizes affects the density as well. The retardation due to crystallization is described by Eq. 2.10 [4],

$$\zeta = \exp(-\beta\chi) \quad (2.10)$$

Where β is a crystalline coefficient that is experimentally shown to be $\beta = 10$ for PA12 [4]. Additionally, χ , is the crystalline fraction. The crystalline fraction depends on whether or not the part is being heated or cooled,

$$\chi(T) = \begin{cases} \chi^H(T), & \text{if heating} \\ \chi^C, & \text{if cooling} \end{cases} \quad (2.11)$$

In the heating phase, the crystalline fraction is a function of the temperature if the temperature is between the initial temperature $T_0 = 175^\circ\text{C}$, and the melting point $T_m = 186.2^\circ\text{C}$ [9],

$$\chi^H(T) = \begin{cases} \frac{c_p(T) - c_p(T_m)}{c_p(T_0) - c_p(T_m)}, & \text{if } T_0 \leq T \leq T_m \\ 0, & \text{if } T > T_m \end{cases} \quad (2.12)$$

At $T \geq T_m$ the crystalline fraction is 0 meaning the polymer is amorphous, and if the crystalline fraction is 1 it means it is fully semi-crystalline.

In the cooling phase, the crystalline fraction is constant and depends on the temperature at the start of cooling,

$$\chi^C = \frac{c_p(T_{C,Start}) - c_p(T_m)}{c_p(T_0) - c_p(T_m)} \quad (2.13)$$

The density during sintering is described by the following relation that takes viscosity, retardation, and crystallinity into account, [21]

$$\frac{d\rho}{dt} = (\rho_{solid} - \rho)\eta_0 \exp\left(-\frac{E_A}{RT} - \beta\chi\right) \quad (2.14)$$

2.1.2 | Thermal Hysteresis

Thermal hysteresis is the phenomenon where a material has a different solidification temperature than the melting temperature. As such you can say that the material properties depend on its thermal history. In an idealized case at the point of melting (or crystallization) all the necessary energy needed for melting, called latent heat, will go into the phase change, and as such the temperature will remain constant until the phase change is complete. Even though, ideally, the temperature isn't increasing the phase transition will cause the total energy content to go up by an amount equal to the latent heat. The total energy content of a system is called the enthalpy, and is denoted by h and has the unit J kg^{-1} . In the real world, however, this transition is not perfectly sharp, and additionally, it is better for the numerical analysis if small transition zones around the melting and solidification temperature are added [5]. Fig. 2.3 shows the thermal hysteresis for PA12, which is based on DSC (differential scanning calorimetry) data from [9]. It shows the melting ($T_m = 186.2^\circ\text{C}$) and solidification temperatures ($T_s = 155.3^\circ\text{C}$) as well as the ends of the transition regions.

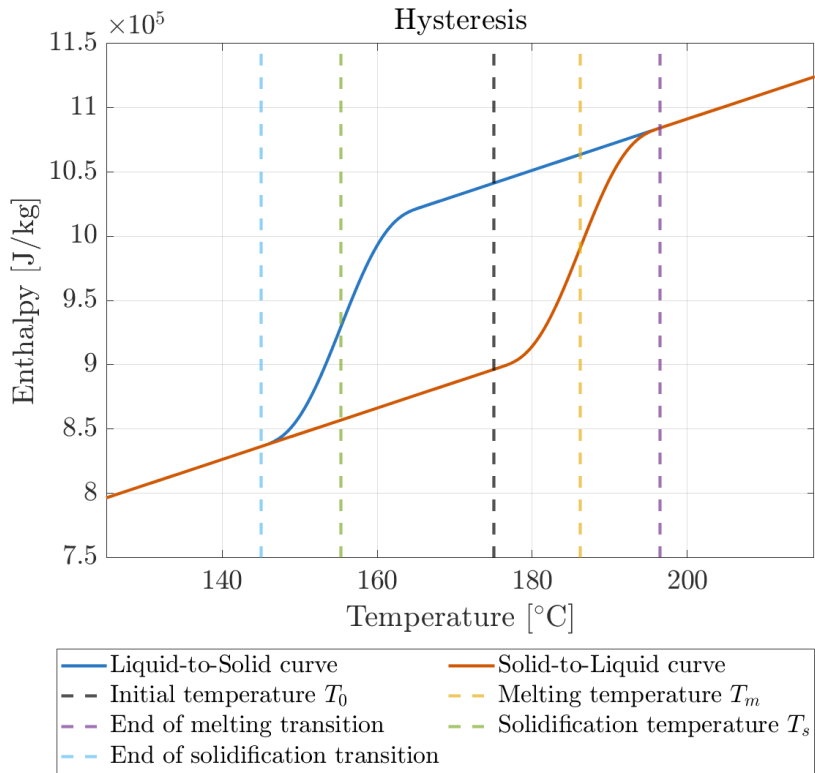


Figure 2.3 | Hysteresis of PA-12

On the Lisa-X SLS 3D printer available at Aarhus University the printer is heated up to an initial temperature of 175 °C. That means that the entire SLS process takes place to the right of the black dashed line in Fig. 2.3, and the material is only allowed to crystallize when the entire print is over and the machine is turned off (cooling phase). If, during heating, the material does not exceed the temperature at the end of the melting transition, then once the heating stops and temperature drops back down to 175 °C it needs to follow a scaled-down liquid-to-solid curve. This is due to the entire latent heat not being fully provided and so the enthalpy isn't high enough to follow the complete liquid-to-solid curve that is depicted in blue in Fig. 2.3. The process of following a scaled-down liquid-to-solid curve is depicted in Fig. 2.4, when moving from Point 1 - Point 2 - Point 3. Additionally in SLS-printing, when a subsequent neighboring layer is heated the sintered layer underneath will heat up a small amount. That is depicted in Fig. 2.4 as moving from Point 3 - Point 4 - Point 5.

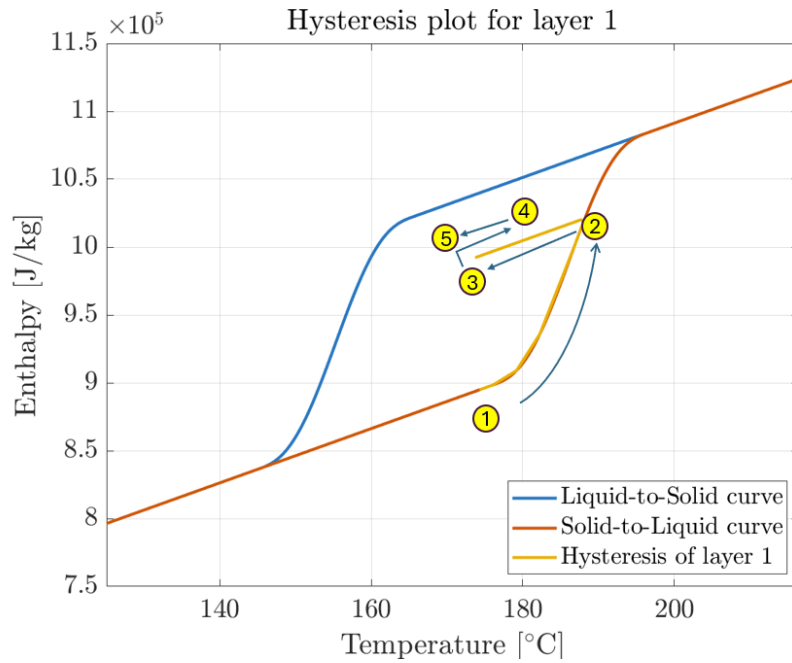


Figure 2.4 | Hysteresis path of layer of PA12 in SLS print

Knowing how the enthalpy changes with temperature, this can be used to compute the specific heat capacity of PA12 using the relation of Eq. 2.15 [Section 4.4, [2]],

$$dh = c_p(T) dT \quad (2.15)$$

2.2 | Flash Heating Simulation

Using the Finite-Element software COMSOL Multiphysics a flash heating simulation of a tensile test specimen, ASTM D638, has been created.

2.2.1 | Applied Heat Source

In flash heating, the laser is not typically modeled as a Gaussian as seen in other work regarding lasers. Instead, the equivalent heat the laser deposits in an entire layer is applied as a volumetric heat source according to the expression [1],

$$q_{FH} = \frac{\xi Q_{active}}{HV_{scan}t_{heat}\delta} \quad (2.16)$$

In Eq. 2.16, δ is the layer height, $\delta = 100 \mu\text{m}$ [20], ξ is the absorptivity which for PA12 is 0.4 [14]. V_{scan} is the scanning velocity which for the Lisa-X is $V_{scan} = 1.1 \text{ m s}^{-1}$, and H is the hatch spacing, $H = 0.3 \text{ mm}$. Q_{active} is the laser power, where the Lisa-X SLS 3D-printer has a max power of $Q_{max} = 15.8 \text{ W}$ and for normal operation the max power is multiplied by an "energy-scaler" of 0.45 [9]:

$$Q_{active} = 0.45 \cdot 15.8 \text{ W} = 7.11 \text{ W} \quad (2.17)$$

t_{heat} is the time a layer is exposed to the heat source and from a simple single-line simulation of a laser with $V_{scan} = 1.1 \text{ m s}^{-1}$, t_{heat} is approximated to be 0.0012s.

Q_{active} represents a completely square wave, and it will be compared to a smoothed square wave, Q_{smooth} , as well as a Gaussian distribution, Q_{gauss} . These different methods are depicted in Fig. 2.5. The equation for the Gaussian is:

$$Q_{gauss} = Q_{active} \cdot \frac{t_{heat}}{\sqrt{2\pi\sigma^2}} \exp\left(-\frac{|t - t_{move}|}{2\sigma^2}\right) \quad (2.18)$$

Where t is the time and t_{move} controls the points around where to center the Gaussian, and as such can be used to control when to apply the laser. σ controls the "spread" of the Gaussian and needs to be chosen such that the entire Gaussian is within the range $t_{start} < t < t_{start} + t_{heat}$. The $Q_{active} \cdot t_{heat}$ scales the Gaussian to ensure the area of Q_{gauss} is the same as Q_{active} . This scaling is also done for Q_{smooth} , as it is important when comparing the three methods that the area under the curve is the same, as this ensures the energy deposited into a layer is the same across all three methods.

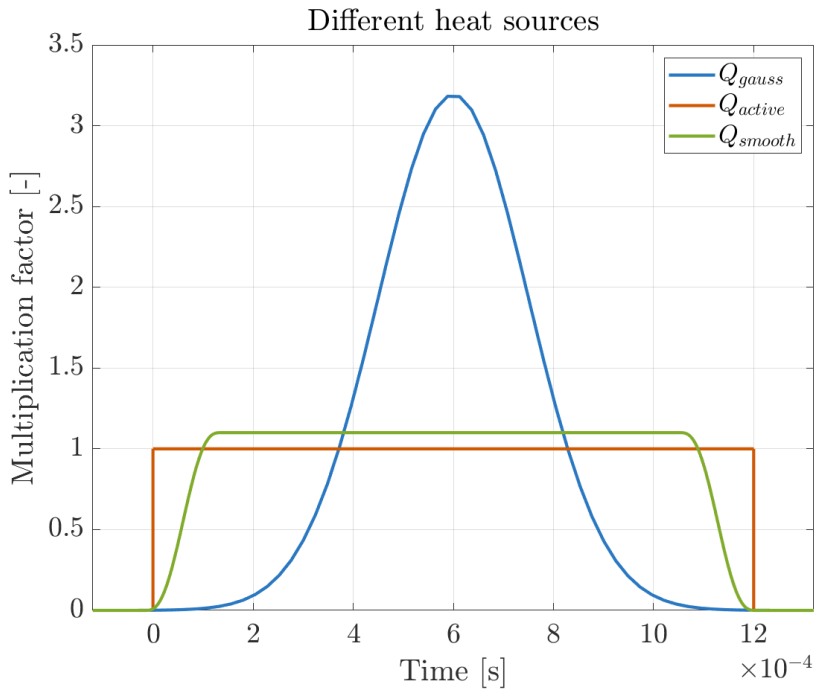


Figure 2.5 | The three different heat sources in time investigated in the simulations

Another issue that needs to be addressed is how to best apply the heat source to the active layer in order for the deactivated layers to remain unaffected. What is done in this study is to change the thermal properties of the deactivated layers to be that of air, since in reality, the top layer would transfer heat into the surrounding air. This means that the deactivated layers above the active layer start to heat up, which presents an issue, as when the time comes for this layer to be activated, the initial temperature will be above that of 175 °C. For this reason, a volumetric heat sink is applied to all deactivated layers using a convection expression as in Eq. 2.7, with the ambient temperature set to 175 °C. The heat transfer coefficient is set to be high enough such that the temperature of the deactivated layer reaches 175 °C before it is that layer's turn to be activated.

2.2.2 | Controlling the Position of the Laser

To create this simulation it is important to be able to control the position of the laser as it moves in steps in the build direction. Note that contrary to most other work the build-direction in this case is set to be the x -direction. To do this the cross-sectional area throughout the part as a function of the position in the build direction, $\text{CSA}(x)$ needs to be determined. This is done by slicing the part in the build plane at numerous points in the build direction and interpolating between these points.

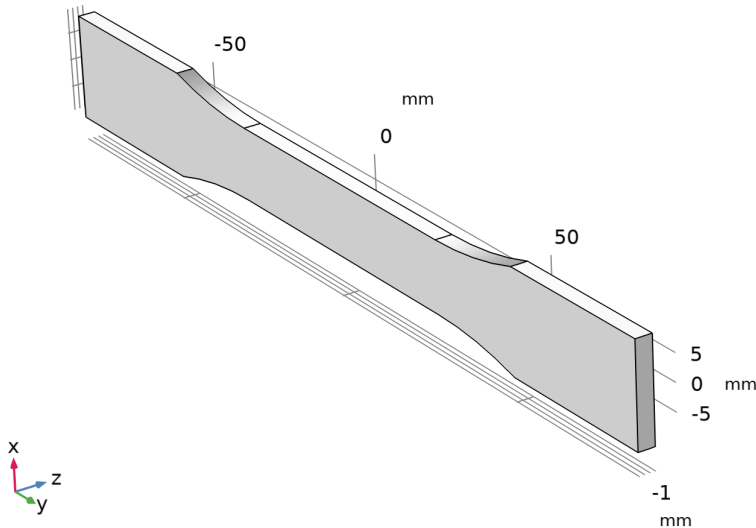


Figure 2.6 | ASTM D638 tensile test specimen

For the ASTM D638 depicted in Fig. 2.6 the cross-sectional area as a function of the height in the build direction is:

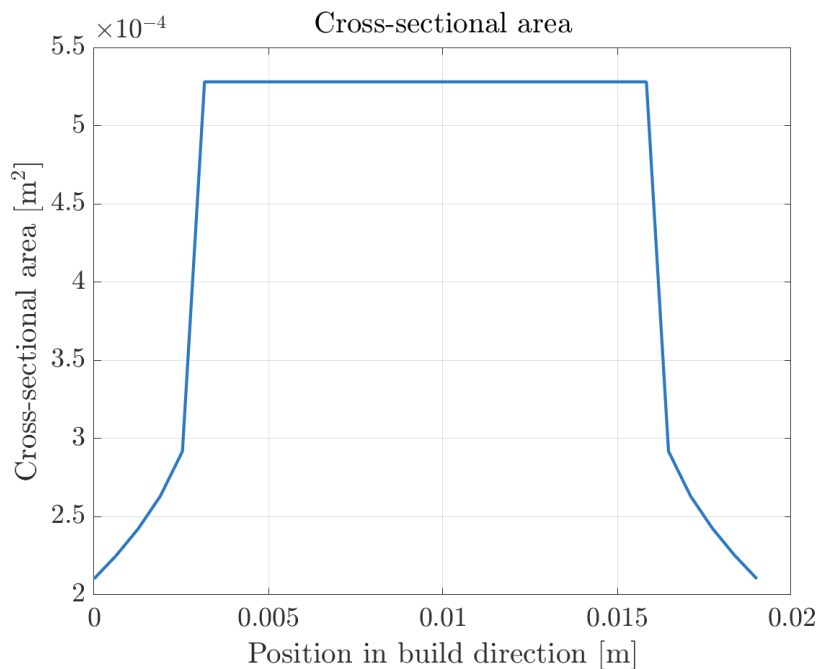


Figure 2.7 | Cross-sectional area in the build-direction

Knowing this the velocity as a function of the position in the build direction can be found.

This is done knowing the height of each layer, the scanning velocity, and the hatch spacing:

$$V_x(x) = \frac{\delta \cdot V_{\text{scan}} \cdot H}{\text{CSA}(x)} \quad (2.19)$$

The position of the laser at any point in time, $x(t)$, as well as the total time of laser scanning can be found by solving:

$$\frac{dx}{dt} = V_x(x) \quad (2.20)$$

Within COMSOL $x(t)$ can be found using an ODE solver.

For the dogbone shown in Fig. 2.6 the laser should move slower in the middle part due to the increase in cross-sectional area. Thus the position of the laser in time $x(t)$ looks like this:

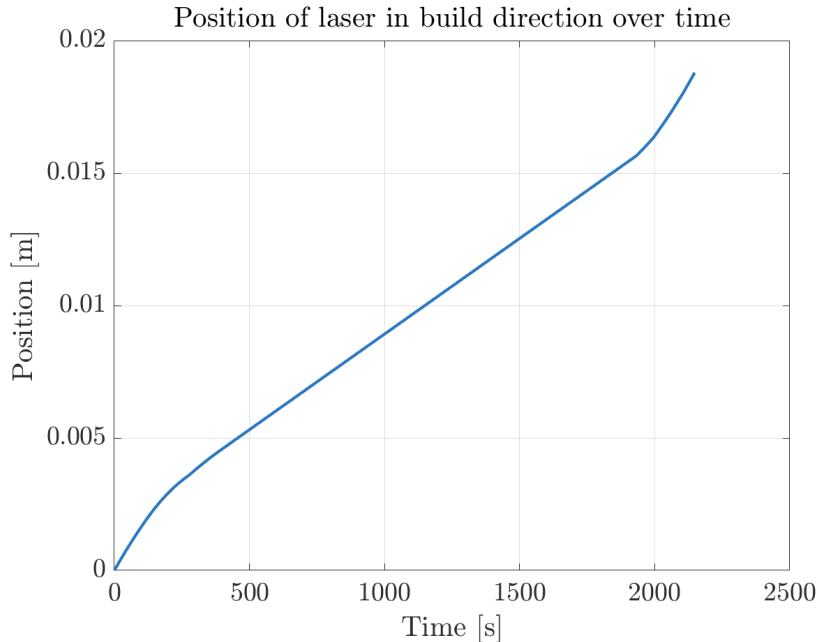


Figure 2.8 | Position of laser over time in build direction

Note that to generate $x(t)$ it is assumed that it takes 10 seconds for each new layer to be deposited. The precise time to deposit a new layer is a task for future work.

Since we want the laser to step layer-by-layer and not continuously, $x(t)$ is then inserted into a stair function that floors the value in between the steps. The length of each step is defined by the height of each layer. This stair function can then be used to control the position of the heat source properly.

2.2.3 | Meshing and Time-stepping

The simulation is run on a dogbone oriented with the build-direction in the thinnest direction (3.2 mm) as this requires the fewest layers, and thus the fastest simulation times. This is depicted in Fig. 2.9.

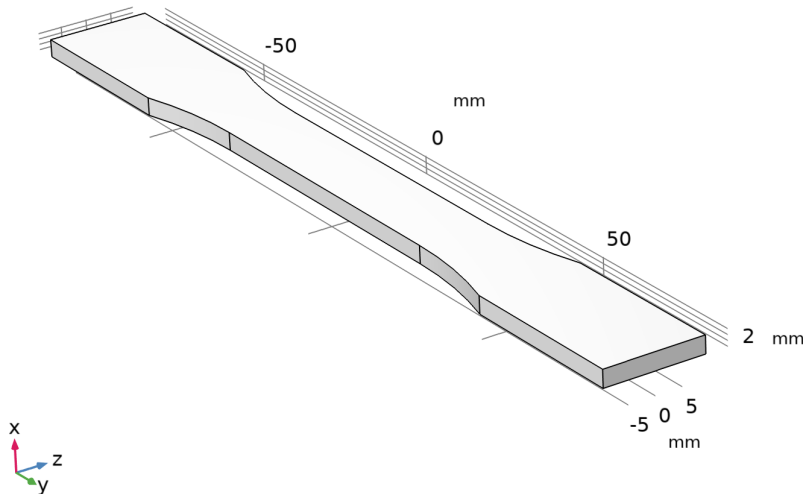


Figure 2.9 | ASTM D638 oriented as simulated

Note that this change in orientation makes the cross-sectional area function constant, and the function for the position of the laser linear.

To ensure easy meshing and to ensure that the number of elements in each layer in the build-direction is the same the part is meshed using identity mapping. This voxelizes the mesh. This makes it so that just the box-shaped build chamber needs to be meshed, which can be meshed easily using quad elements. The effect of two different mesh distributions in the build-plane, a coarse and a fine mesh, and the effect of two different mesh distributions in the build direction (1 or 2 elements) has been investigated. The coarse mesh without the dogbone is depicted in the zy -plane in Fig. 2.10, and the mesh used for the identity mapping is shown in Fig. 2.11. Note that both figures depict meshes in 3D viewed from the top.

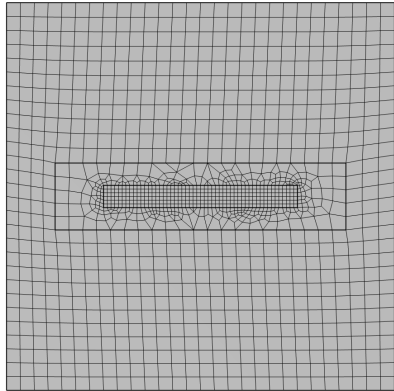


Figure 2.10 | Coarse mesh without dogbone

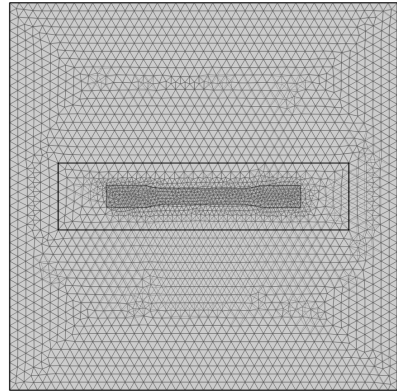


Figure 2.11 | Mesh for identity mapping

The mesh with the dogbone for the identity mapping isn't what the simulations use for the calculations, and as such its refinement isn't important as long as it captures the shape of the part decently.

The other mesh, the fine mesh is depicted in Fig. 2.12.

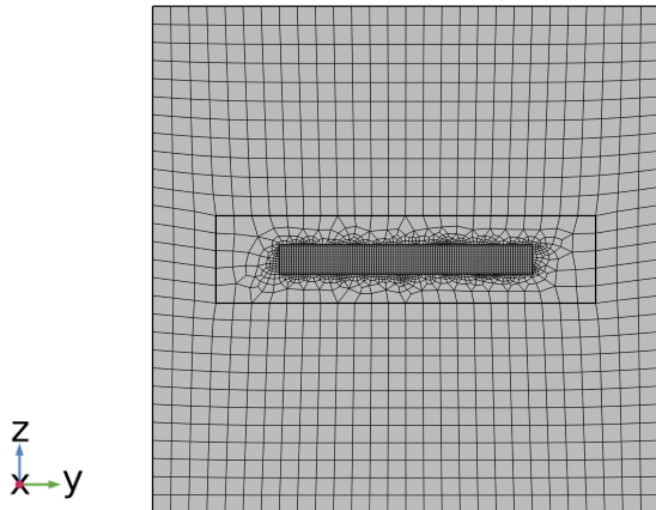


Figure 2.12 | Top view of 3D mesh: Fine mesh without dogbone

As mentioned the mesh in the build-direction is either with 1 element per layer or 2 elements per layer. The number of elements per layer and the number of layers affects the time-stepping of the simulation. To ensure accurate results in the simulation the Courant number is used [Section 6.3.1, [\[7\]](#)]

$$C = V_x \cdot \frac{\Delta t}{\Delta x} \quad (2.21)$$

Where $\Delta x = L_x/N_{ele}$ is the spatial grid spacing.

The Courant-Friedrich-Lowy condition of $C \leq 1$ is imposed to ensure numerical stability. This is done even though this condition is mostly used for explicit time-stepping schemes, and an implicit scheme, which is normally unconditionally stable, is used in this study. However in this case, when working with a moving heat source the condition of $C \leq 1$ is important to ensure that a time-step does not skip over elements.

From the CFL condition, the maximum time step can be found:

$$\Delta t = \frac{L_x}{V_x \cdot N_{ele}} \quad (2.22)$$

3 | Results and Discussion

The 3D temperature distributions are depicted in Fig. 3.1 at four moments in time, which are the moments corresponding to the maximum temperature in each layer. The subplots are all sectioned along the y -axis, so the internal temperature of the dogbone is visible.

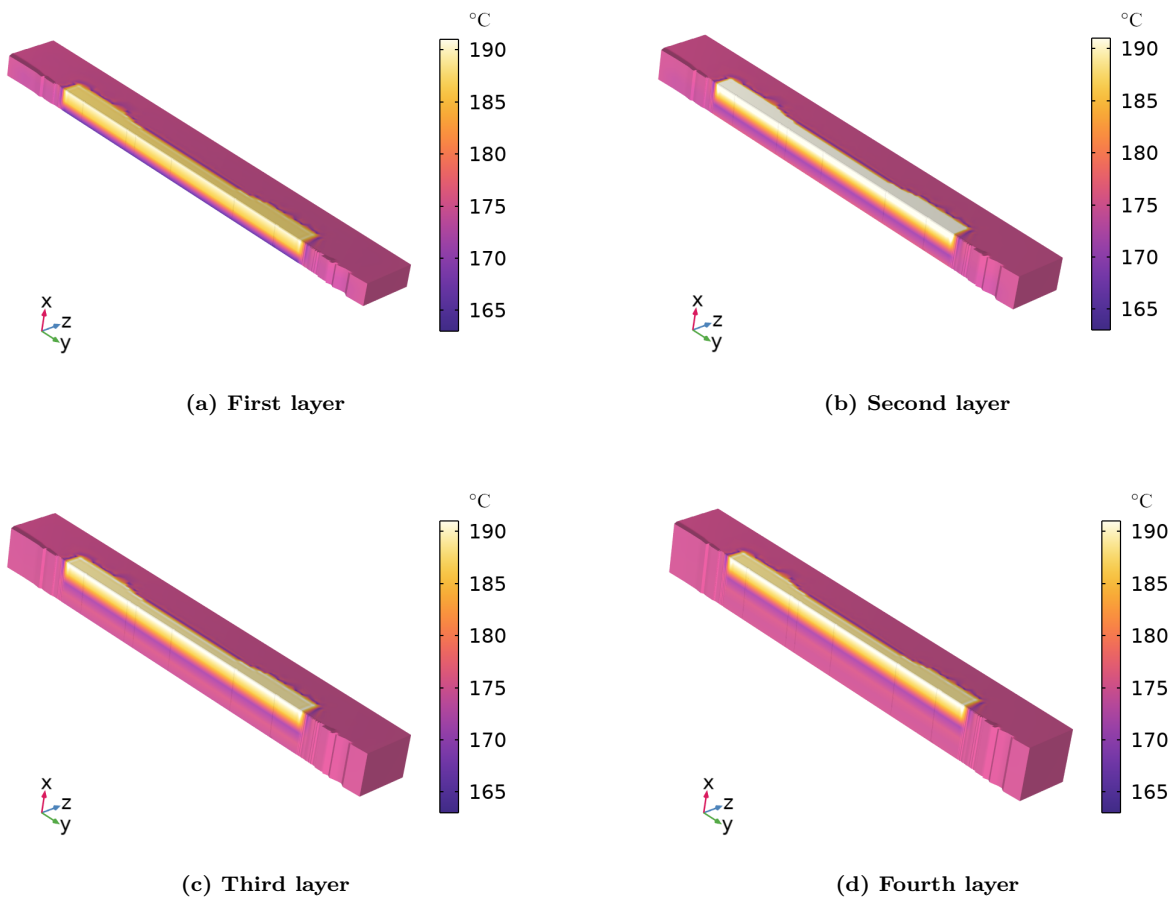


Figure 3.1 | Section-view of the layer-by-layer temperature distribution of the flash heating process for 4 layers in total. The x -axis has been scaled by a factor of 7 for visual clarity

Note that all simulations are performed on a laptop with an Intel(R) Core(TM) i7-9750H CPU and 16 GB of RAM.

In Fig. 3.1 4 layers are sintered in the simulation in total. The ASTM D638 tensile test specimen has a thickness in the chosen x -direction of 3.2 mm, since the real layer height is 100 μm , then, in reality, it would take 32 layers to print, which would be computationally expensive. To save time, 4 layers in total are simulated, which means that 8 real layers are being printed simultaneously.

Fig. 3.1 shows that subsequent layers get flash heated as time passes. The temperature at the center of each layer is shown in Fig. 3.2

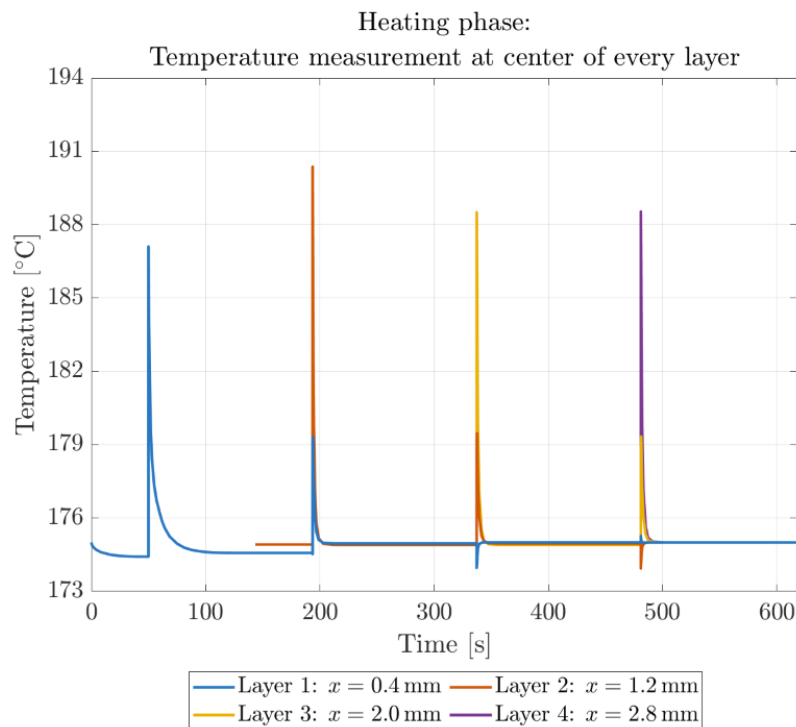


Figure 3.2 | Heating phase temperature at the center of every layer of the baseline simulation. Each layer is plotted from the time just before the layer is activated to the end time. That is why only the first layer is active at $t = 0$

Each layer experiences a sharp temperature peak, and then gradually cools down in between layers. For all the simulations a general tendency is for the first layer to have the lowest temperature peak. This is suspected to be due to the first layer not having any sintered layers underneath, and therefore it doesn't conduct heat downwards in the same way the remaining layers do. A small dip in temperature can be observed for example for layer 1, when layer 3 gets activated. This is assumed to be a product of the numerical

method, and as long as the dips are small they are assumed to be insignificant.

Once the heating phase is over, the cooling phase begins in which the ambient temperature of the convection boundary conditions change to 20 °C. The temperature at the center of each layer in the cooling phase is depicted in Fig. 3.3

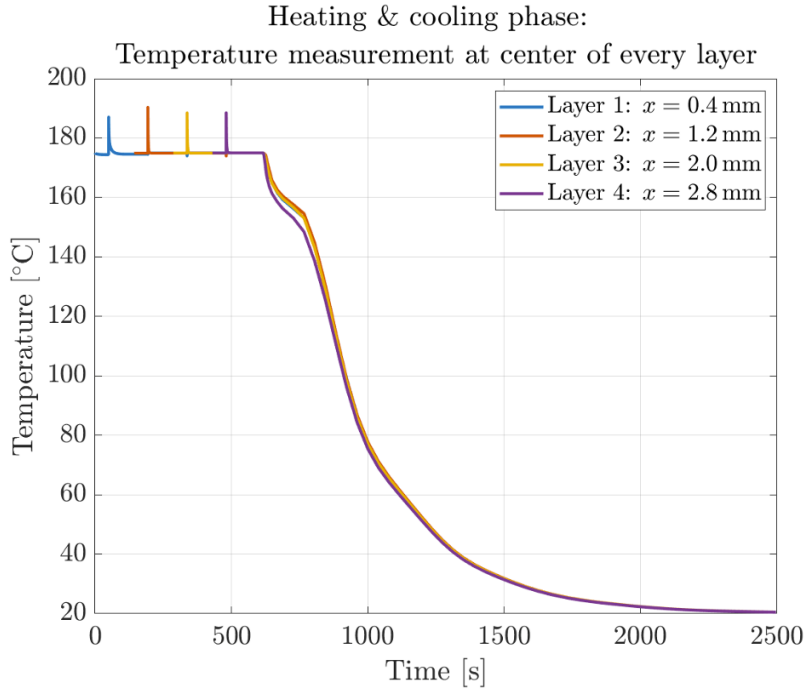


Figure 3.3 | Heating & cooling phase temperature at center of every layer of the baseline simulation

In both the heating and the cooling phase each layer needs to follow the thermal hysteresis curve correctly. The first layer presents no issue, and it follows the thermal hysteresis curve exactly as predicted in Fig. 2.4. However, an issue with the hysteresis poses for all the other layers. In Figs. 3.2 and 3.3, the part of each plot that occurs before a layer is activated is omitted. That is why in Fig. 3.2 only layer 1 starts at $t = 0$. However, before activation, the layer consists of air that experiences temperature rises due to the heating of layers underneath. Fig. 3.4 depicts the entire heating phase for the third layer.

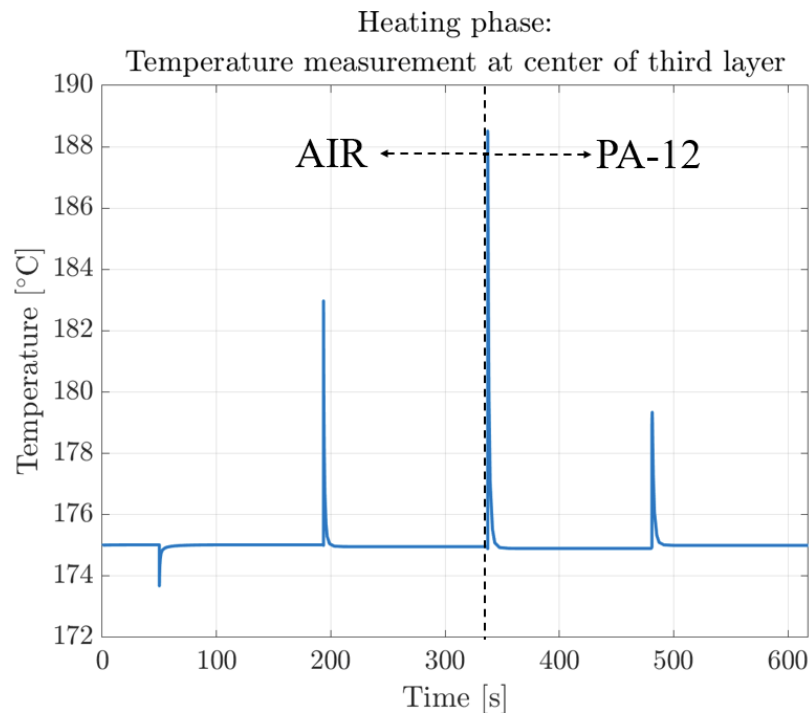


Figure 3.4 | Temperature over time of third layer

Which has the corresponding thermal hysteresis that is depicted in Fig. 3.5.

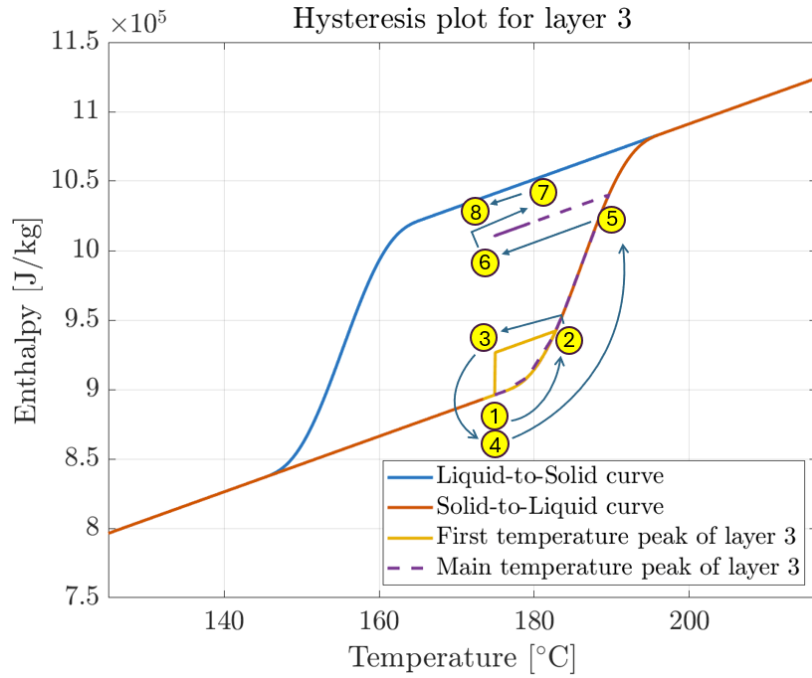


Figure 3.5 | Hysteresis path of layer 3. The hysteresis is being reset from point 3 to point 4

As such the first minor temperature peak at $t \approx 200$ s in Fig. 3.4 causes the movement from Point 1 to Point 2 and then it cools to Point 3 in Fig. 3.5. However, to ensure that once the major temperature peak at $t \approx 320$ s occurs that the enthalpy doesn't start from Point 3, the enthalpy needs to be reset to the initial value at Point 4 (same point as Point 1). From there the hysteresis curve can be followed for the major peak just like for the first layer. This reset is important to implement.

3.1 | Simulation Setting Analysis

Finding the optimal simulation settings is important to ensure accurate results at fast simulation speeds. For this study, the effect of tweaking the following simulation settings has been investigated:

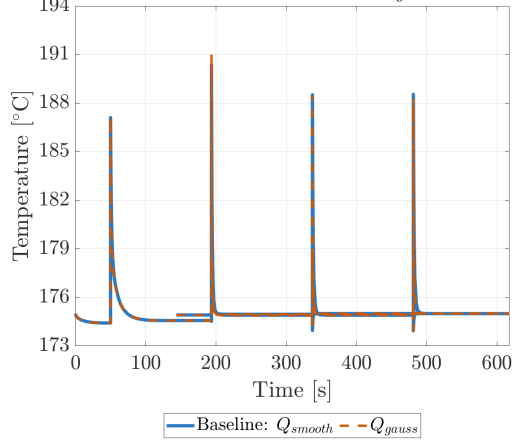
- Type of applied heat source: Square (Q_{active}), smoothed square (Q_{smooth}), or Gaussian (Q_{gauss})
- Discretization: Linear or quadratic serendipity
- The exposure time: $t_{heat} = 0.0012$ s or $t_{heat} = 0.012$ s
- Build-plane meshing: Coarse (Fig. 2.10) or fine (Fig. 2.12)
- Elements in build-direction: 1 or 2 elements
- The number of layers, N_o : 4 or 8.

For each simulation setting the mean value and the standard deviation of the peak temperatures in each layer as well as the simulation time have been logged. The relative tolerance has been altered for every simulation setting to provide good results at fast simulation times.

Both Figs. 3.1 to 3.5 depict the heating phase of the simulation which serves as the baseline. The baseline has the following settings: Q_{smooth} , linear discretization, $t_{heat} = 0.0012$ s, the coarse mesh, 1 element in build direction, and $N_o = 4$. In Figs. 3.6 and 3.7 the baseline is compared to all the tweaked simulation settings.

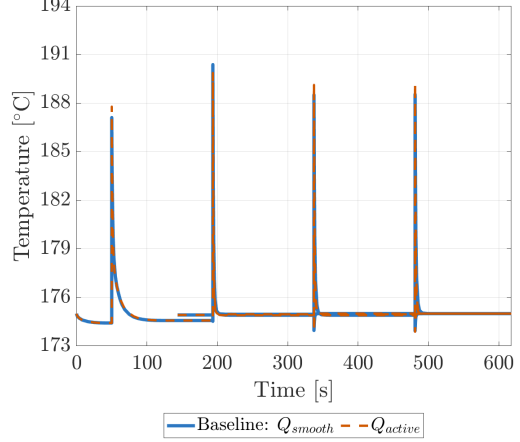
CHAPTER 3. RESULTS AND DISCUSSION

Heating phase: Temperature at center of every layer
comparing Q_{smooth} and Q_{gauss}



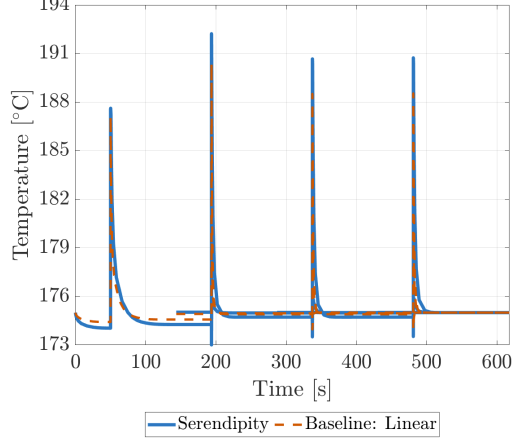
(a) First layer

Heating phase: Temperature at center of every layer
 Q_{smooth} compared to Q_{active}



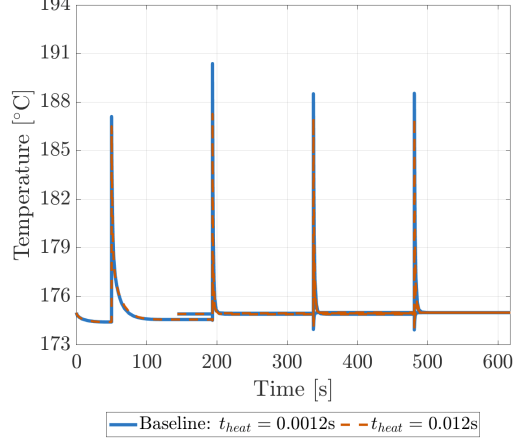
(b) Second layer

Heating phase: Temperature at center of every layer
Comparing discretizations



(c) Third layer

Heating phase: Temperature at center of every layer
Comparing values of t_{heat}



(d) Fourth layer

Figure 3.6 | Results for the first four settings in the settings analysis

CHAPTER 3. RESULTS AND DISCUSSION

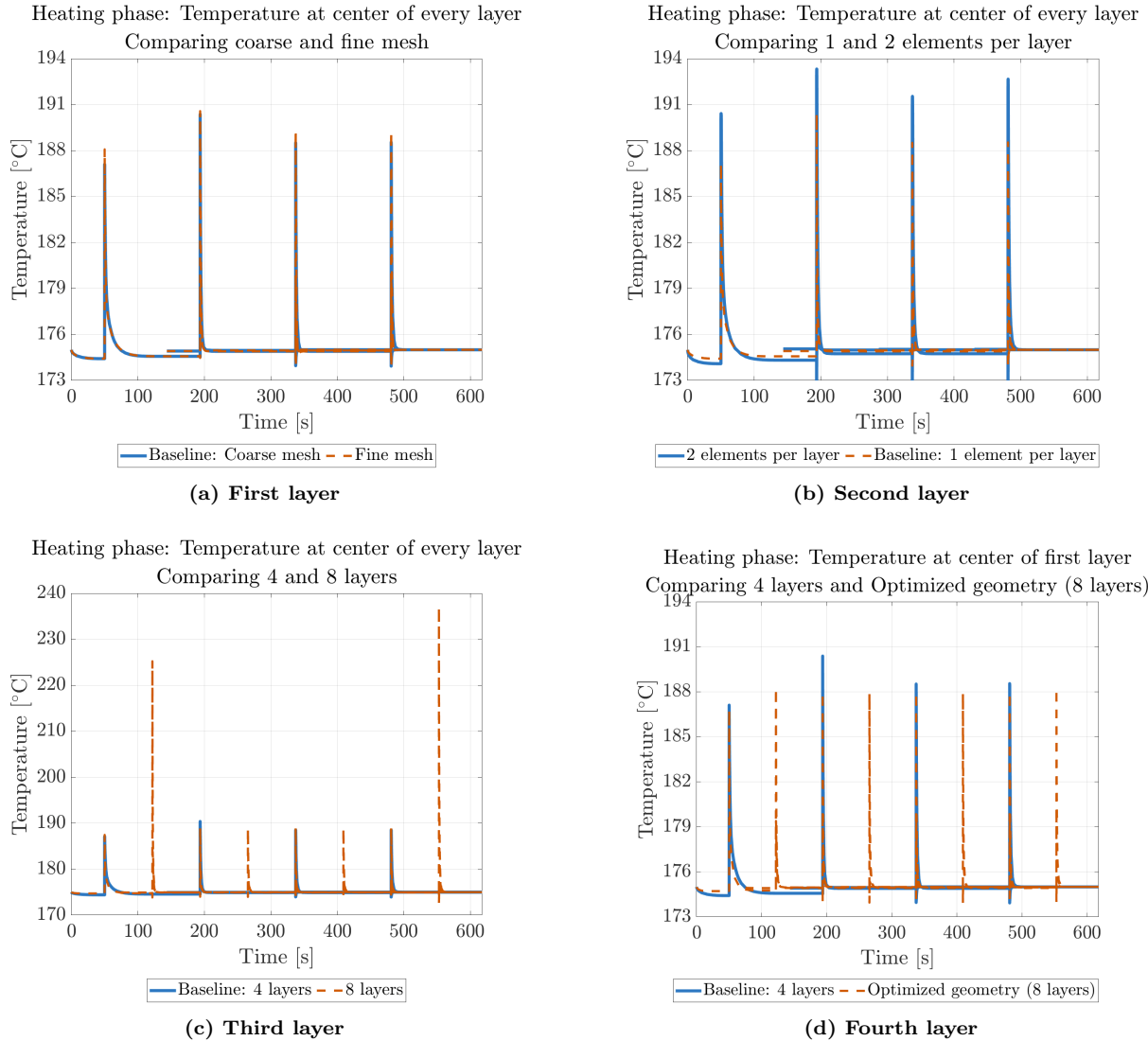


Figure 3.7 | Results for the last four settings in the settings analysis

For the baseline the simulation takes 4 min 16 s to run, the mean of the peak temperature of each layer is 188.636 °C and the standard deviation of the peak temperature of each layer is 1.340 °C. These values have been inserted along with the same values for every other simulation in Table 3.1.

Changed parameter compared to baseline	Average [°C]	Standard Deviation [°C]	Time	Figure ref.
Baseline	188.636	1.340	4min 16s	3.2
Q_{gauss}	188.708	1.635	5min 45s	3.6a
Q_{active}	189.026	0.879	4min 24s	3.6b
Quadratic serendipity	190.311	1.933	7min 24s	3.6c
$t_{\text{heat}} = 0.012\text{s}$	186.954	0.321	3min 16s	3.6d
Fine mesh	189.272	1.022	13min 45s	3.7a
2 elements per layer	191.985	1.278	32min 30s	3.7b
$N_o = 8$ & Fine mesh	199.252	19.929	27min 45s	3.7c
Optimized geometry*	187.837	0.447	26min 53s	3.7d

Table 3.1 | Results for every simulation. *The optimized geometry consists of Q_{smooth} , linear discretization, $t_{\text{heat}} = 0.012\text{s}$, fine meshing, 1 element in build direction, and $N_o = 8$

For the optimized geometry, which has Q_{smooth} , linear discretization, $t_{\text{heat}} = 0.012\text{s}$, fine meshing, 1 element in build direction, and $N_o = 8$, 3D plots of the density distributions have been created:

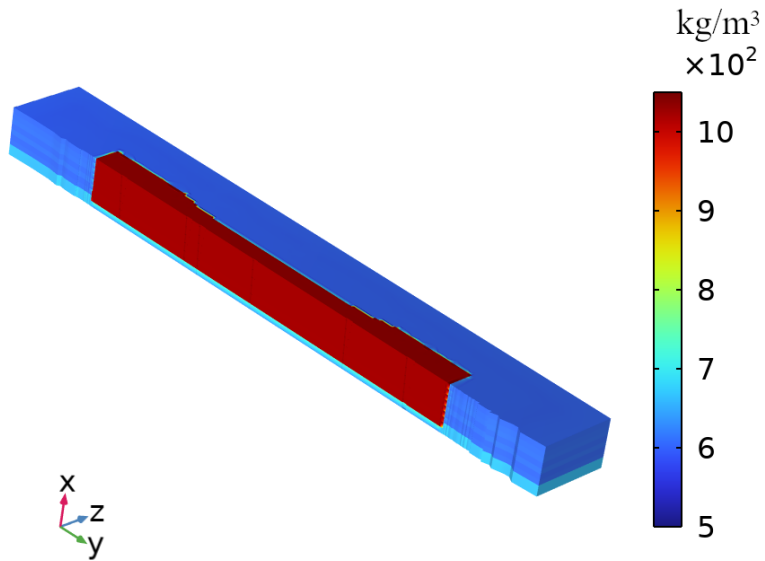


Figure 3.8 | Section view of the density in the 'Optimized geometry'. The x -direction is scaled with a factor of 5

From the simulation setting analysis, it can be concluded that the model is quite robust. Qualitatively from Figs. 3.6 and 3.7 the temperature distribution are very similar across all settings. This is confirmed quantitatively in Table 3.1, where it can be seen that for all settings the found averages and standard deviations lie very close to one another. In most cases, the slight differences that are seen in standard deviations and averages, such as for " Q_{gauss} " and "Quadratic serendipity" can probably be attributed to the relative tolerance not being low enough. But in general, as long as a sufficient relative tolerance is chosen all but the setting " $N_o = 8\%$ Fine mesh" produces viable results, and the most interesting factor to use for comparing the settings is the simulation time:

- Comparing the three heat source methods the findings are that Q_{gauss} tends to have a slightly longer computation time. This is possibly due to the fact that Q_{gauss} has a sharp peak that requires more time-stepping to properly resolve.
- Linear discretization produces the quickest results compared to quadratic serendipity discretization.
- As expected refining the mesh in the build-plane increases the computational time significantly. This doesn't affect the result average or standard deviation significantly but obviously affects the 'resolution' of the simulated part.
- Adding an additional element per layer vastly increases computational times, whilst not improving results. The average tends to be a bit higher for 2 elements per layer compared to baseline, this is suspected to be due to how the results are probed. The results are probed in the center of each layer, as such when there are 2 elements per layer the results are probed exactly at a node. When there is only 1 element the results are probed in between nodes. As such it might be better in the future to consider an average temperature across the layer height when comparing the effects of adding more elements per layer.
- An interesting finding is that increasing t_{heat} by a factor of 10, seems to cause the standard deviation to lower, and possibly the average to lower a bit as well. However, this cannot be thoroughly concluded. Each layer is still being heated the correct amount as the amount of energy deposited into each layer is the same regardless of the exposure time. It is theorized, however, that there is a limit to how much you can increase t_{heat} , as increasing it too much will affect how much time a layer has to cool before the next layer is activated. As such t_{heat} should always be much smaller than the cooling time in between layers. Increasing t_{heat} does cause the computation time to go down, which is assumed to be caused by the solver being better able to step through the heating phase. Increasing the exposure time has proven to be useful to improve cases where the solver struggled to step correctly through the heating events when $t_{heat} = 0.0012\text{ s}$ such as for " $N_o = 8\& \text{ Fine mesh}$ ", which is

depicted in Fig. 3.7c. Increasing the exposure time of " $N_o = 8$ & Fine mesh" by a factor of 10 is what was done to create an "Optimized" model.

The purpose of the "Optimized" model was to get a general idea of the computational time of a full model, that has a sufficiently fine mesh with a sufficient amount of layers to be able to properly resolve the thermomechanical model to get the residual stresses that is the goal of the author's Master's thesis. For the reasons listed, the following settings were chosen for an "Optimized" model: Q_{smooth} , linear discretization, $t_{heat} = 0.012$ s, fine meshing, 1 element in build direction, and $N_o = 8$. With these settings, the simulation time is 26 min and 53 s. The temperature at the center of each layer for the optimized model is depicted in Fig. 3.7d, where it can be seen that the temperature peaks are stable.

4 | Future work

This subject will be continued in the author's Master's thesis in spring 2025. The warping and curling that occur in SLS printing due to uneven thermal shrinking and expansion are significant to understanding the process of SLS and being able to minimize the failure rate of printed parts. The future work entails the inclusion of the mechanical problem to compute the elastic, viscoplastic, thermal, and residual strains and stresses that occur when SLS printing. To do this it will be necessary to investigate the boundary conditions as the part isn't fixed but instead surrounded by powder that only partly inhibits warping. Future work could also include crystallization kinematics, or different models for describing the changing material properties such as the experimentally based density model used in [17], that take density hysteresis into account. Additionally, experimental validation of the model will be needed to know how accurately the model captures the stresses and strains. For the experimental validation, it will be important to tune the simulation to the exact parameters of the Lisa-X printer, as in this study the exact way the ambient temperature ramps down in the cooling phase, as well as the exact cooling time in between layers in the heating phase has been estimated. Finally, it might prove useful both for accuracy and for speeding up the simulations to implement adaptive meshing strategies.

5 | Conclusion

This study aimed to create a flash heating model of an SLS print process. This resulted in an easy-to-use model that can be easily tweaked to fit a specific thermal problem of any geometry with the desired material properties.

The model takes into account the important phase changes that occur in SLS printing, among which thermal hysteresis and changing viscosity, porosity, and crystallinity affect the material properties of the material. The robustness and computational speed of the model were prioritized to create a good foundation for the model for future work which will entail adding the ability of the model to predict residual stresses. To optimize the robustness and computational speed an investigation of a wide range of parameters has been performed. The parameters are; the type of heat source applied, the discretization, the heat exposure time, separately the refinement of the mesh in the build plane and the build direction, and the number of layers in the print process.

It was found that the model generally is very robust and produces results very close to one another for almost all the chosen parameters. For this reason, the simulation time is the parameter of interest.

- It was found that a heat source applied as a square wave or smoothed square wave produced the quickest simulation times compared to a Gaussian.
- Linear discretization produces faster results than quadratic serendipity.
- Extending the heat exposure time (from $t_{\text{heat}} = 0.0012 \text{ s}$ to $t_{\text{heat}} = 0.012 \text{ s}$), was shown to produce more robust results in some cases.
- Refining the mesh in the build place increases the computational time and doesn't produce more accurate results. It does however increase the resolution of the simulated part, and for that reason, a sufficiently fine mesh will be important when moving on to simulating residual stresses.
- Adding more mesh elements in each layer was shown to increase computational time drastically, whilst not producing better results.

For an optimized geometry that is thought to produce results that are sufficiently refined to capture residual stresses, the simulation time was found to be 26 min and 53 s. This is

CHAPTER 5. CONCLUSION

thought to be sufficiently fast for this to be a viable method for continuing the work in the author's Master's thesis on using flash heating to capture residual stresses. If significantly larger or vastly more refined parts need to be analyzed more computational power will be needed. For this, the computational cluster available at Aarhus University can come in handy.

6 | Bibliography

- [1] M. BAYAT, C. G. KLINGAA, S. MOHANTY, D. DE BAERE, J. THORBORG, N. S. TIEDJE, AND J. H. HATTEL, *Part-scale thermo-mechanical modelling of distortions in laser powder bed fusion – analysis of the sequential flash heating method with experimental validation*, Additive Manufacturing, 36 (2020).
- [2] Y. A. CENGEL, M. A. BOLES, A. J. GHAJAR, AND M. KANOĞLU, *Thermodynamics An Engineering Approach*, McGraw Hill, 9th ed., 2019.
- [3] Y. A. CENGEL AND A. J. GHAJAR, *Heat and Mass Transfer - Fundamental & Applications*, McGraw Hill, 2014.
- [4] T. H. C. CHILDS, C. HAUSER, C. M. TAYLOR, AND A. E. TONTOWI, *Simulation and experimental verification of crystalline polymer and direct metal selective laser sintering*, in 2000 International Solid Freeform Fabrication Symposium, 2000.
- [5] COMSOL, *Thermal modeling of phase change materials with hysteresis*, 2016. <https://www.comsol.com/blogs/thermal-modeling-of-phase-change-materials-with-hysteresis> [Accessed: 28-11-2024].
- [6] L. DONG, A. MAKRADI, S. AHZI, AND Y. REMOND, *Three-dimensional transient finite element analysis of the selective laser sintering process*, Journal of Materials Processing Technology, 209 (2009), pp. 700–706.
- [7] J. H. FERZIGER, M. PERIC, AND R. L. STREET, *Computational Methods for Fluid Dynamics*, Springer, 4th ed., 2020.
- [8] I. GIBSON, D. ROSEN, B. STUCKER, AND M. KHORASANI, *Additive Manufacturing Technologies*, Springer, 3rd ed., 2014.
- [9] J. HESSELVIG AND R. T. NYGAARD, *Studying sls-printing through multiphysics thermal and flow analysis with experimental validation*, 2024. Bachelor's Project.
- [10] R. M. JONES, *Mechanics of Composite Materials*, Tayler & Francis, 2nd ed., 1999.
- [11] S. KALPAKJIAN AND S. R. SCHMID, *Manufacturing Engineering and Technology*, Pearson, 8th ed., 2020.
- [12] P. KOSKY, R. BALMER, W. KEAT, AND G. WISE, *Chapter 12 - mechanical*

- engineering*, in Exploring Engineering, P. Kosky, R. Balmer, W. Keat, and G. Wise, eds., Academic Press, Boston, third edition ed., 2013, pp. 259–281.
- [13] C. LI, S. E. SNARR, E. R. DENLINGER, J. E. IRWIN, M. F. GOUGE, P. MICHALERIS, AND J. J. BEAMAN, *Experimental parameter identification for part-scale thermal modeling of selective laser sintering of pa12*, Additive Manufacturing, 48 (2021), p. 102362.
 - [14] P. PEYRE, Y. ROUCHAUSSE, D. DEFAUCHY, AND G. RÉGNIER, *Experimental and numerical analysis of the selective laser sintering (sls) of pa12 and pekk semi-crystalline polymers*, Journal of Materials Processing Technology, 225 (2015), pp. 326–336.
 - [15] D. RIEDLBAUER, M. DREXLER, D. DRUMMER, P. STEINMANN, AND J. MERGHEIM, *Modelling, simulation and experimental validation of heat transfer in selective laser melting of the polymeric material pa12*, Computational Materials Science, 93 (2014), pp. 239–248.
 - [16] C. SARAF, *The ultimate guide for selective laser sintering (sls): Process, materials, applications, advantages, disadvantages*, (July 2024).
 - [17] F. SHEN, W. ZHU, K. ZHOU, AND ET AL., *Modeling the temperature, crystallization, and residual stress for selective laser sintering of polymeric powder*, Acta Mechanica, 232 (2021), pp. 3635–3653.
 - [18] SINTERIT, *Pa12-industrial material's technical data sheet*, 2022. <https://sinterit.com/wp-content/uploads/2022/11/PA12-Industrial.pdf>, [Accessed: 12-06-2024].
 - [19] SINTERIT, *Sinterit Lisa X Original User Manual*, March 2022. https://sinterit.com/wp-content/uploads/2021/12/Sinterit_LisaX_OryginalUserManual_EN_032022.pdf, [Accessed: 12-06-2024].
 - [20] SINTERIT, *Sinterit lisa x product specification*, 2022. https://sinterit.com/wp-content/uploads/2023/05/LisaX_specification_EN.pdf, [Accessed: 12-06-2024].
 - [21] A. E. TONTOWI AND T. H. C. CHILDS, *Density prediction of crystalline polymer sintered parts at various powder bed temperatures*, Rapid Prototyping Journal, 7 (2001), pp. 180–184.
 - [22] Z.-D. ZHANG, S. IMANI SHAHABAD, O. IBHADODE, C. F. DIBIA, A. BONAKDAR, AND E. TOYSERKANI, *3-dimensional heat transfer modeling for laser powder bed fusion additive manufacturing using parallel computing and adaptive mesh*, Optics Laser Technology, 158 (2023), p. 108839.

Declaration of use of GAI tools

I/we used generative artificial intelligence (GAI) to complete this project
(*tick the box*). List the GAI tool(s) you used (remember to specify version):

- ChatGPT 3.5
- ChatGPT 4

I/we used GAI tools in the following way (*See accompanying list of possible uses for inspiration*)

- For feedback on own text
- For alternative ways of formulating text
- To understand a topic better
- For programming tasks, such as creating the code that plots figures in MATLAB.